Mechanical characterization of diesel soot nanoparticles: in situ compression in a transmission electron microscope and simulations

Istvan Zoltan Jenei, Fabrice Dassenoy, Thierry Epicier, Arash Khajeh, Ashlie Martini, Dairene Uy, Hamed Ghaednia, Arup Gangopadhyay

Mechanical characterization of diesel soot nanoparticles: in situ compression in a transmission electron microscope and simulations

Istvan Zoltan Jenei[1,5,6], Fabrice Dassenoy[1,6], Thierry Epicier[2], Arash Khajeh[3], Ashlie Martini[3,6], Dairene Uy[4,6], Hamed Ghaednia[4] and Arup Gangopadhyay[4]

1 Ecole Centrale de Lyon, LTDS, 36 Avenue Guy de Collongue F-69134, Ecully, France
2 Université de Lyon, INSA-Lyon, MATEIS, UMR5510 CNRS, 7 Avenue Jean Capelle, F-69621, Villeurbanne Cedex, France
3 Department of Mechanical Engineering, University of California Merced, Merced, CA 95343, United States of America
4 Powertrain Research and Advanced Engineering, Ford Motor Company, Dearborn, MI 48124, United States of America

Abstract

Incomplete fuel burning inside an internal combustion engine results in the creation of soot in the form of nanoparticles. Some of these soot nanoparticles (SNP) become adsorbed into the lubricating oil film present on the cylinder walls, which adversely affects the tribological performance of the lubricant. In order to better understand the mechanisms underlying the wear caused by SNPs, it is important to understand the behavior of SNPs and to characterize potential changes in their mechanical properties (e.g. hardness) caused by (or during) mechanical stress. In this study, the behavior of individual SNPs originating from diesel engines was studied under compression. The experiments were performed in a transmission electron microscope using a nanoindentation device. The nanoparticles exhibited elasto-plastic behavior in response to consecutive compression cycles. From the experimental data, the Young's modulus and hardness of the SNPs were calculated. The Young's modulus and hardness of the nanoparticles increased with the number of compression cycles. Using an electron energy loss spectroscopy technique, it was shown that the sp2/sp3 ratio within the compressed nanoparticle decreases, which is suggested to be the cause of the increase in elasticity and hardness. In order to corroborate the experimental findings, molecular dynamics simulations of a model SNP were performed. The SNP model was constructed using carbon and hydrogen atoms with morphology and composition comparable to those observed in the experiment. The model SNP was subjected to repeated compressions between two virtual rigid walls. During the simulation, the nanoparticle exhibited elasto-plastic behavior like that in the experiments. The results of the simulations confirm that the increase in the elastic modulus and hardness is associated with a decrease in the sp2/sp3 ratio.

E-mail: istvan.jenei@mmk.su.se, fabrice.dassenoy@ec-lyon.fr, amartini@ucmerced.edu and duy@ford.com

[5] Present address: Department of Materials and Environmental Chemistry, Stockholm University, 106 91 Stockholm, Sweden.
[6] Authors to whom any correspondence should be addressed.

Keywords: soot nanoparticle, compression, molecular dynamics, *in situ* TEM

1. Introduction

One of the major concerns of the automotive industry is reduction of friction and wear between the moving parts of a vehicle. These tribological improvements not only lower the running cost of a vehicle and increase its operational life, but also have a beneficial effect on the environment through lower emissions. The low carbon emissions of internal combustion engines are controlled by strict environmental regulations. One way to conform to these regulations is to develop sophisticated injection systems in engines. However, an undesired effect of the use of direct injection systems is an increase in the production of of soot nanoparticles (SNPs) in the combustion chamber. Recently, advances in turbocharged direct injection engines have optimized the combustion scheme to minimize soot generation [1]. However, the mechanical properties of soot particles are one key to understanding the effect of soot contamination on lubricant properties.

SNPs are a byproduct of incomplete fuel (hydrocarbon) combustion. Thus they mainly comprise carbon, but hydrogen can also be found in soot at a concentration of approximately 1 wt%, which leads to the empirical formula C_8H [2]. Soot production could originate in the premature quenching of fuel droplets in the combustion chamber (cylinder). Since SNPs are formed in the cylinders they can contain trace elements which originate from engine oil additives or small wear debris [3]. Some of the SNPs are evacuated into the exhaust system, but a fraction of them can be adsorbed into the thin oil film which lubricates the cylinder walls.

Previous transmission electron microscope (TEM) investigations have revealed that soot is composed primarily of typically spherical particles having diameters of a few tens of nanometers, although the primary particles easily form aggregates that can have diameters of several hundred nanometers [3–8]. Previous computer simulations have shown the formation of primary soot particles with a diameter of about 15 nm, as well as a wide range of morphologies during agglomeration [9]. The primary particle has an outer shell and a core. X-ray diffraction (XRD) techniques indicate that the carbon atoms of SNPs are arranged into hexagonal face-centered arrays or platelets, which in turn form layers [10]. The outer shell is composed of such layers. The inner core is chemically and structurally less stable due to the thermodynamic instability of its structure [10, 11]. Uy *et al* characterized diesel and gasoline turbocharged direct injection (GTDI) SNPs from the morphological and chemical point of view [3]. It was found that GTDI soot either has a turbostratic structure typical of diesel soot or it appears sludge-like. The authors suggested in their study that this difference in the morphology of diesel and GTDI soot can lead to differences in the hardness of the SNPs, which can affect the wear mechanisms inside the engine.

The tribological properties of the lubricating oil can be altered by the presence of SNPs. Models exist which can predict the effect of nanoparticles on a lubricant's performance based on the mechanical behavior of a single nanoparticle [12]. Due to the formation of soot agglomerates, the oil viscosity might change [13], which can lead to pumpability problems and, eventually, increased friction [14]. The presence of SNPs in the oil may change anti-wear properties as well [15–17]. Several soot-related wear mechanisms have been proposed [16]: large soot agglomerates cause lubricant starvation in the contact; the SNPs reduce the ability of the anti-wear additive to protect the surface; and the primary SNP, due to its hardness, is able to abrasively wear the contact surface. Recently, Motamen Salehi *et al* [18] found that consumption of engine oil additives by SNPs (additive adsorption) has a significant effect on the wear of different engine components. It should be mentioned that the above-cited studies refer to diesel SNPs or carbon black. In order to better understand the wear mechanisms caused by the SNPs in engine oil, it is important to first understand their mechanical and chemical properties.

Since the late 1990s *in situ* TEM techniques have been developed to perform nanomechanical tests such as compression, tensile straining and nanoindentation on nano-objects in the microscope [19, 20]. With the development of commercial microelectromechanical systems (MEMS), such as the Nanofactory Instruments AB holder [21], or Hysitron systems [22], *in situ* TEM techniques have become invaluable tools in materials science (see for example a recent review in [23]). With such tools, the mechanical properties of a large variety of nanotubes, nanoparticles, nanowires, micro-pillars and even surfaces and coatings have been studied [24–31].

The work by Lahouij *et al* [29] is of special interest for the present work. Those authors studied the behavior of primary SNPs and agglomerates originating from a diesel engine when an external load is applied using a nanoindentation device. They found that, under compression, the primary SNPs exhibit elasto-plastic behavior, and they don't show damage after compressions of up to 7 GPa contact pressure. The elastic behavior of the single particle was reflected in the behavior of the agglomerate. Lahouij *et al* also found that primary SNPs, as well as agglomerates, are able to roll under shear conditions.

In this article, SNPs originating from diesel engines were studied. The objective was to measure and analyze the mechanical properties of single SNPs at the nanoscale. In order to achieve this, a series of *in situ* compression tests were performed on individual SNPs using a commercially available nanoindentation device (manufactured by Hysitron, Inc.) inside a TEM. TEM imaging provided structural information about the nanoparticles before and after compression. Based on the data provided by the nanoindentation device and the TEM images, Young's moduli and hardness values were reported. Recording electron energy loss spectra of the SNPs

Table 1. Information about the SNPs used in the experiments.

Sample reference	Engine type	Soot source
D1	Diesel	Vehicle test
D2	Diesel	Engine dynamometer test
D3	Diesel	Vehicle exhaust

allowed calculation of the sp^2/sp^3 ratio. A correlation was observed between this ratio and the behavior of the nanoparticles under consecutive compression. Molecular dynamics simulations of soot compression were also performed, which enabled investigation of the origin of the trends in the elastic modulus and hardness. Gaining information about the mechanical properties of the SNPs could provide better understanding of the mechanism of the wear they induce in engines.

2. Experimental

2.1. Soot nanoparticles

The SNPs were extracted from diesel engine oils. The nanoparticles were washed out using hexane in a centrifugation procedure; this is described in more detail in [8]. The origin of the studied SNPs is reported in table 1.

2.2. TEM

The nanocompressions of the SNPs were performed in a FEI C_s corrected Titan environmental transmission electron microscope (ETEM) operating at an accelerating voltage of 300 kV. The images and movies of the compression experiments were recorded using a Gatan OneView camera.

Electron energy loss spectroscopy (EELS) was performed with a GIF Tridiem spectrometer. All spectra were recorded with the 1 mm entrance aperture and with a dispersion of 0.05 eV per channel. The spectrometer was used in diffraction coupling mode.

Working with SNPs made it crucial to minimize as much as possible the potential carbon contamination during the experiments. For this, the following steps were taken: the ETEM was used in a 'high vacuum' mode with an active liquid nitrogen cold-trap, ensuring a pressure in the 10^{-8} mbar range. All analyses were performed with a small condenser aperture ($d = 50\ \mu$m) and a small spot size 6. The dose rate in compression experiments was ≈163 electrons $Å^{-2}\ s^{-1}$ while the total dose for a typical experiment (accounting for three consecutive compressions) was ≈44 000 electrons $Å^{-2}$. These parameters for the the EELS measurements were ≈2700 electrons $Å^{-2}\ s^{-1}$ and ≈146 000 electrons $Å^{-2}$, respectively. Prior to any observation, a beam-shower was performed at low magnification with a moderate beam intensity.

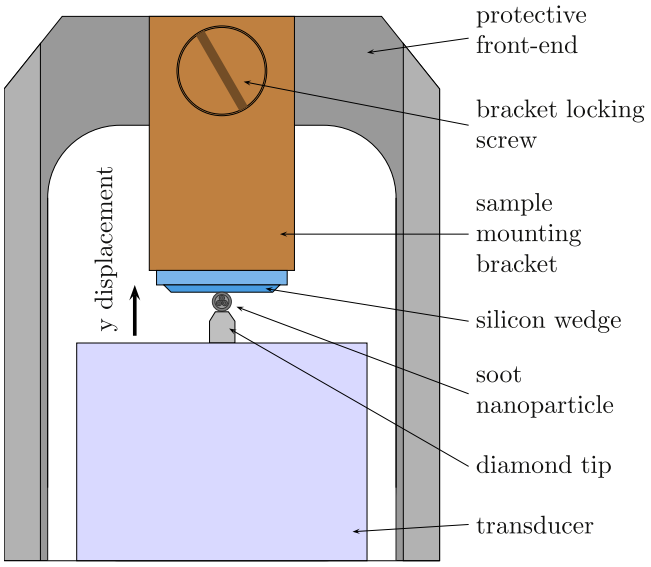

Figure 1. Schematic representation of the PI95 picoindenter performing a compression test on a single SNP.

2.3. Picoindenter

The nanocompressions were carried out using a Hysitron PI95 picoindenter, a special TEM sample holder, the front end of which is schematically represented in figure 1. The main component of the picoindenter is the transducer: a sharp diamond tip having a cube corner geometry attached to a MEMS device. The device used in these experiments is a so-called 1D transducer, which is capable of measuring forces in one direction (along its main axis of symmetry); the force measurement resolution is 3 nN and the maximum measurable force is 1 mN. The picoindenter enables three levels of motion control: 3D mechanical control in the micrometer to millimeter range; 3D piezo control in the nanometer to micrometer range; and 1D computer control in the sub-nanometer range with a resolution of 0.02 nm.

The SNPs were deposited on the plateau of the silicon wedge using the following method. The soot powder was suspended in cyclohexane, with a concentration of less than 0.05 wt%. Prior to sample preparation, the suspension was sonicated for at least 15 min. A strand of hair was dipped into the suspension and then it was wiped on the plateau area of the silicon wedge in a longitudinal direction. A new silicon wedge was used for every experimental session.

An example of SNP compression can be seen in figure 2(a). The diamond tip was brought towards the nanoparticle, without making contact. After aligning the tip with the nanoparticle, a displacement control test was initiated: the tip was set to move in the y direction (as specified in figure 2(a)) at a constant rate of $1\ \text{nm}\ s^{-1}$. When the pre-set maximum displacement was reached, a pause of 2 s followed, after which the tip was retracted at a speed of $2\ \text{nm}\ s^{-1}$. The control function, which governs the motion of the tip during compression, is illustrated in figure 2(b). The pre-set displacement was tailored to the size of the nanoparticle (it varied between 10 and 30 nm in the experiments presented in

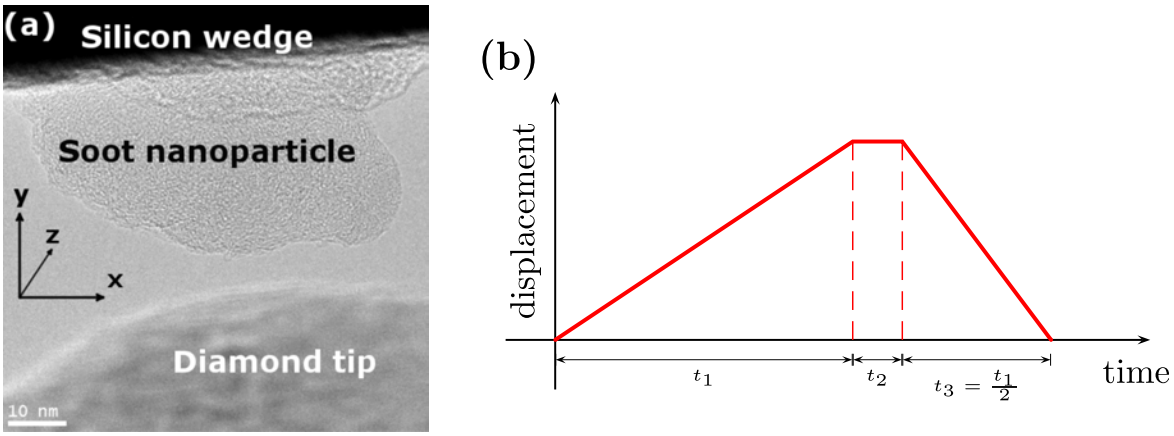

Figure 2. (a) A TEM image of a SNP before compression. (b) The control function used during the compression tests.

this study). During a compression test, the position of the tip (on the y axis), the force detected by the tip in the y direction and a video captured from the display screen were recorded. Thus, a force–displacement curve was obtained, which could be correlated to the video of the compression sequence. Before and after each compression, a TEM bright-field image was recorded giving access to morphological characteristics such as the (two-dimensional) size of the tested particle.

2.4. Young's modulus and hardness calculations

In order to calculate the Young's modulus directly, the SNP/diamond tip contact area is required. Given the composition and geometry of the experimental setup, this was not possible. However, the contact surface could be approximated by the area of a circular disk, assuming a semi-axisymmetric particle geometry. The diameter of the disk (d_A), as viewed 'edge-on', was measured from the appropriate frames of the compression videos. It was then chosen to systematically approximate every contact surface in this way. By using this approximation, an uncertainty is added to the calculations, which would be difficult to quantify. For this reason, no proper error propagation was performed. In order to calculate the Young's modulus of the nanoparticle during a compression test, only the elastic behavior needs to be considered. For elasto-plastic behavior, the unloading section contains purely elastic contributions, so:

$$\frac{F_{\max}}{A} = E\frac{l}{t} \tag{1}$$

where $F_{\max}$ is the maximum force measured during the compression, A is the contact area, $A = \pi d_A^2/4$, d_A being the diameter of the contact, E is the Young's modulus, l is the size change measured as a result of the elastic behavior of the nanoparticle and t is the y-size of the particle at maximum compression (at the point where $F_{\max}$ is measured). Figure 3 illustrates these parameters. From equation (1) the Young's modulus can be expressed as

$$E = \frac{4\,F_{\max}\,t}{\pi\,d_A^2\,l}. \tag{2}$$

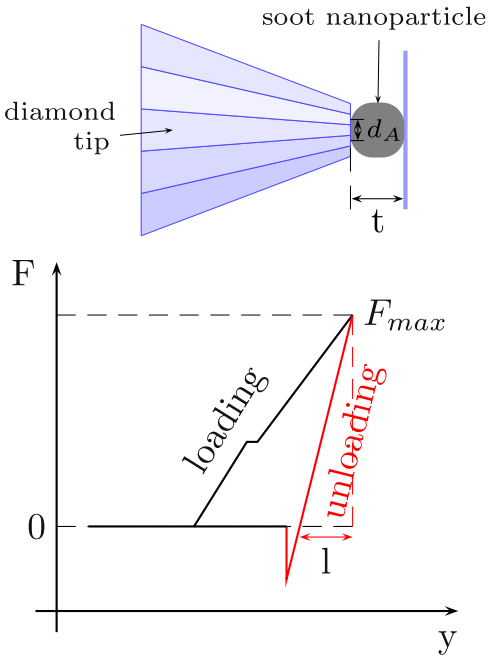

Figure 3. Illustration of the parameters used in the calculations of Young's modulus and hardness.

When making the linear least squares fit to the data points corresponding to the unloading, a relation between the displacement, y, and the measured force, $F_{\max}$, can be written as $F_{\max}/l = b$, b being the slope of the fitted line. Using this, the Young's modulus can be written as

$$E = \frac{4\,t\,b}{\pi\,d_A^2}. \tag{3}$$

Parameters t and d_A can be read from the frame-shot captured from the compression video, and b can be obtained from the slope of the $F(y)$ function.

The hardness of the particle can be calculated as follows:

$$H = \frac{F_{\max}}{A} = \frac{4\,F_{\max}}{\pi\,d_A^2}. \tag{4}$$

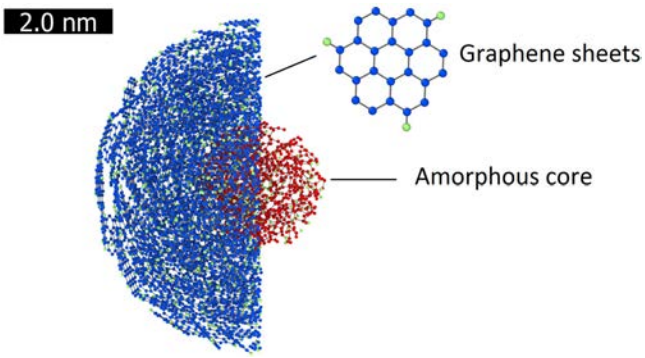

Figure 4. Structure of the model soot particle consisting of an amorphous core and a graphitic shell. Red and blue spheres indicate carbon atoms in the amorphous core and graphitic shell, respectively. Light green spheres correspond to hydrogen atoms.

3. Simulations

The experimental measurements were complemented by molecular dynamics (MD) simulation. Figure 4 illustrates the components of the model particle: an amorphous core and a graphitic shell consisting of 450 graphene flakes. Previous studies reported a range of 20–30 nm for the size of a primary SNP which is composed of an amorphous core with a diameter of 8–15 nm and a graphitic shell with a thickness of 4–12 nm [5, 6, 29, 32]. This approximately 1 to 1 ratio of the core size to the shell thickness was reproduced in the MD simulations by scaling down the core diameter and shell thickness to 2.1 nm each. The amorphous core was created through a process of heating carbon atoms up to 5000 K for 10 ps, followed by a quenching step to room temperature at a rate of 0.5 K fs^{-1}. Subsequently, hydrogen atoms were added to the system at randomly generated positions to obtain a 1:8 carbon to hydrogen ratio, and then a constant-temperature simulation was run until the potential energy of the system was stable. The graphene layers used for modeling the outer shell were composed of 24 carbon atoms and 3 hydrogen atoms which preserve the 8:1 carbon to hydrogen atom ratio reported in previous publications [10]. PACKMOL software [33] was employed to create parallel stacked graphene layers and combine them with the amorphous core into a single model. Surface oxidation was neglected in the model particle. During all simulations, the interactions between atoms were modeled using the reactive force-field ReaxFF [34, 35] with parameters developed for a Pt/Ni/C/H/O system [36]. The ReaxFF potential has been used in previous simulations to model the formation of a soot particle [37].

To equilibrate the system, thermal equilibrium simulations under the *NVT* ensemble (constant number of atoms, volume and temperature) were performed with the model nanoparticle in a large simulation box at 300 K for 10 ps. The result was a nearly spherical particle with a core density of 2.1 g cm^{-3} and a graphitic shell in which the average interlayer spacing between graphene flakes was 0.31 nm. These two parameters are in good agreement with the previously reported values for diesel soot [10, 38, 39].

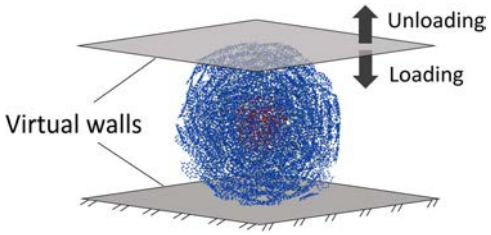

Figure 5. Schematic of compression simulations using two virtual walls at the top and bottom of the modeled particle.

Once equilibrated, the nanoparticle was subject to repeated compression cycles. Figure 5 shows a schematic of the compression simulations. Two virtual walls at the top and bottom of the particle were defined, where the interactions between the walls and the atoms in the nanoparticle were modeled using a 9-3 Lennard-Jones potential with parameters $\epsilon = 0.043$ eV and $\sigma = 0.1$ nm, and a cutoff distance of 0.2 nm. Three consecutive compression tests were simulated. During the loading and unloading stages, the lower wall was fixed and the upper wall was moved at a speed of 40 m s^{-1}. At each loading stage, the nanoparticle was compressed until its height decreased to 40% of the initial value, and then unloading was performed until the net force acting on the upper wall was zero. All the MD simulations were performed using the software LAMMPS (Large Atomic/Molecular Massively Parallel Simulation) [40]. During each compression cycle, the force–displacement diagram, sp^2/sp^3 carbon atom ratio, and hardness were recorded. To calculate the hardness value, the maximum force acting on the upper wall at the end of loading stages was used in equation (4).

4. Results and discussion

Figure 6(a) shows a TEM bright-field image of a SNP (D1). This particle is round in shape, having dimensions of 23 and 26 nm in the x and y directions, respectively. The outer shell and the inner core structure of the particle can be distinguished (as described in [6]). The particle is sitting on the silicon wedge. It can be seen from the contrast of the image that the material deposit (supposedly carbonaceous material) obscuring the SNP is not at the same height as the nanoparticle and thus does not affect its behavior during compression (further details are available in the online supporting information).

A displacement control test was initiated with a maximum displacement of 15 nm. The recorded compression and the force–displacement curve can be seen in the first supplementary video (available online at stacks.iop.org/NANO/29/085703/mmedia). Unfortunately, there was a small, unintended drift in the motion of the tip. A TEM image after the first compression is shown in figure 6(b). The recorded force–displacement measurements for this compression are shown in figure 7(a). It can be observed that the particle exhibits elasto-plastic behavior during the compression. In figure 7(a) the green and red lines represent linear least squares fits to the loading and unloading data.

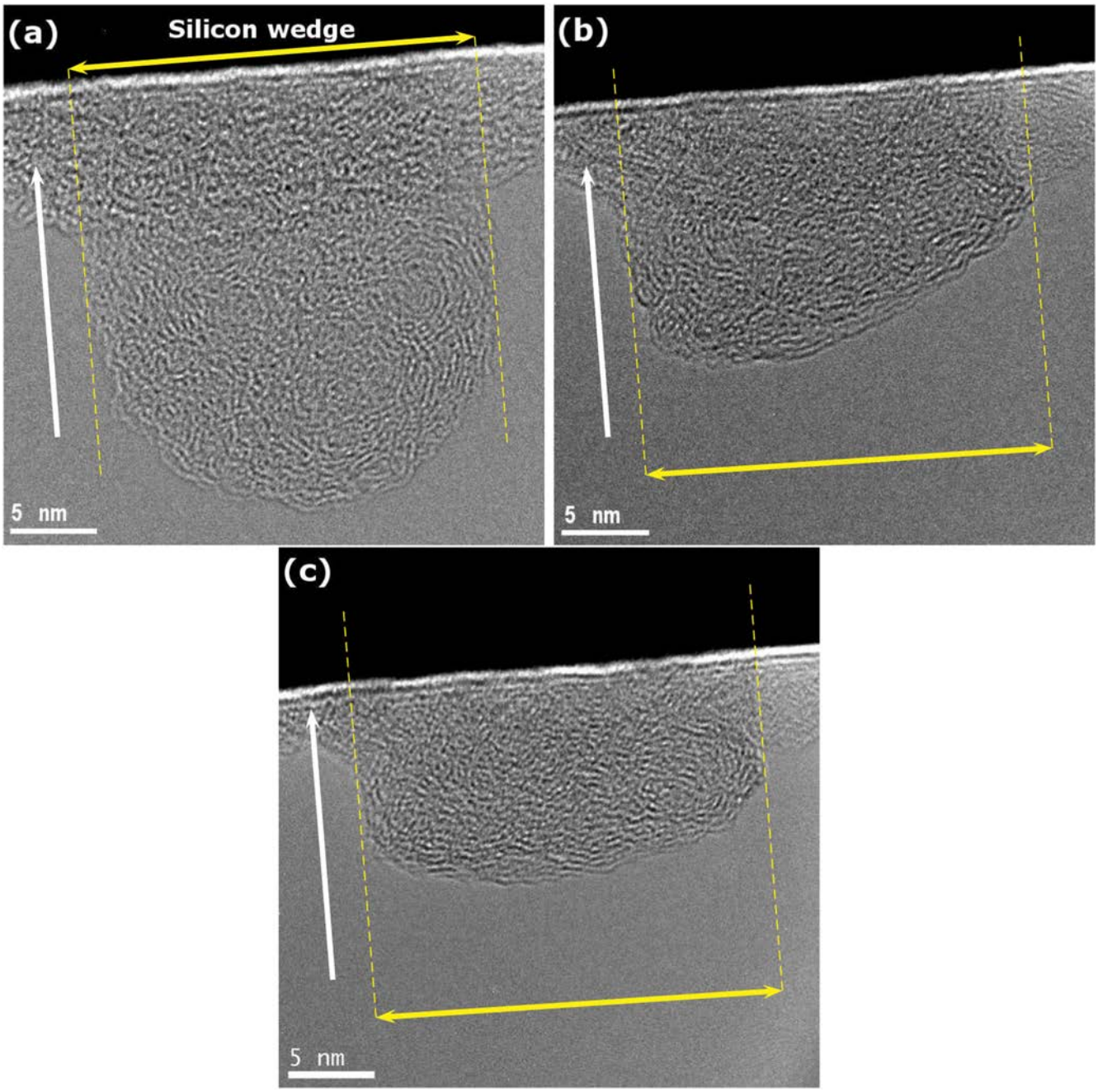

Figure 6. TEM images of a soot nanoparticle (a) before, (b) after the first and (c) after the second compression. The *x*-size of the particle remains relatively unchanged (the length indicated with a yellow line is constant in all the subfigures). The white arrow indicates the *y* displacement (direction of compression).

A second compression with the same parameters was performed, and the compression can be seen on the second supplementary video. The TEM image of the particle after the second compression is shown in figure 6(c). The recorded force–displacement data and the linear least squares fit to the loading and unloading sections can be seen in figure 7(b).

After these two consecutive compressions, several observations can be made. First, the particle suffered a permanent change in size. While its *x*-size remained relatively unaltered (23 nm before, 22 nm after the first and 23 nm after the second compression; see these indicated *x*-sizes in figure 6), the *y*-size of the particle changed considerably (from 26 nm before, to 16 nm after the first and 12 nm after the second compression). The change in *y*-size after the second compression corresponds to a ≈50% decrease compared with the original size of the particle.

The structure of the particle also changed. As can be seen in figure 6, the exterior layers of the outer shell of the particle were 'smoothed', and also became more aligned to the direction perpendicular to the direction of compression. This alignment was also observed in the simulations from visual analysis of the graphite flakes. Lastly, the turbostratic and fullerenoid structure of the core of the particle has almost disappeared.

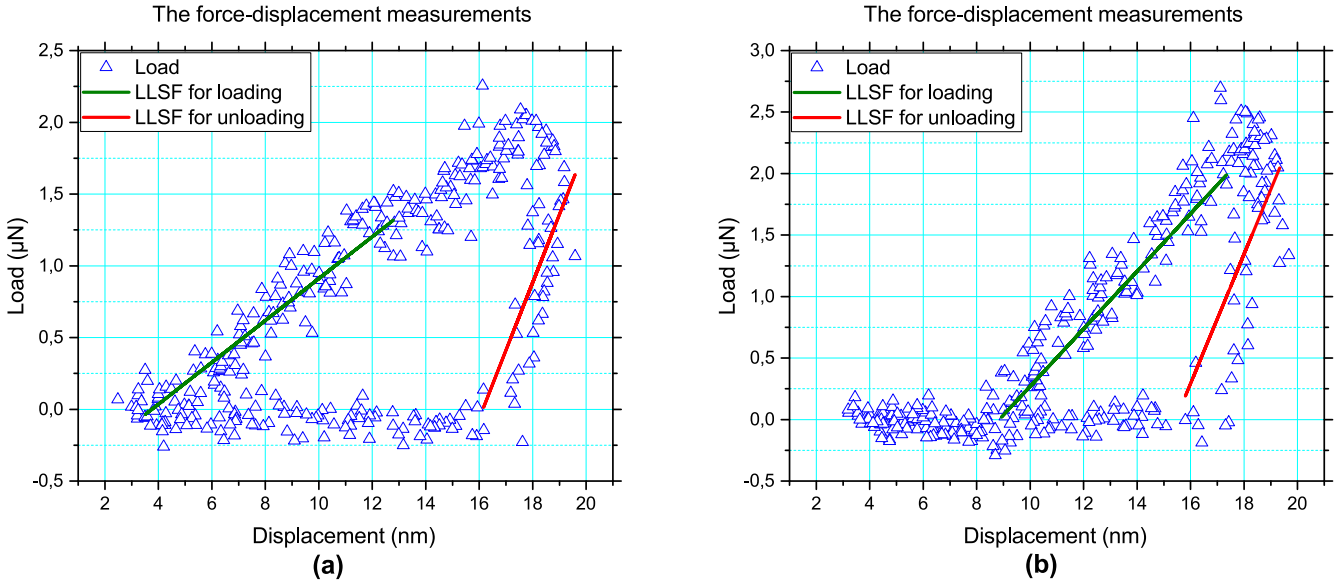

Figure 7. (a) The recorded force–displacement data from the first compression with linear least squares fits to the data points during loading and unloading. (b) The recorded force–displacement data for the second compression with linear least squares fits to the data point during loading and unloading.

The same elasto-plastic behavior was observed during compression as that reported by Lahouij *et al* [29]. Those authors described that a single compressed nanoparticle is able to withstand pressures up to 7 GPa without suffering major structural damage. In the present work, the SNPs were subjected to higher contact pressures (up to 16 GPa, as shown later), and, while no particle break-up was observed after the compression, the nanostructure of the soot particles changed.

Another parameter that can be calculated from the force–displacement data is the slope of the fitted line. This slope characterizes the behavior of the particle during compression, which can be related to elastio–plastic contributions during loading and to elastic contributions during unloading. This slope during the unloading part is referred to as an 'elastic constant'. It can be seen that the 'elastic constant' of the particle increased from 0.473 μN nm^{-1} for the first compression to 0.527 μN nm^{-1} for the second compression.

Based on equations (3) and (4), the Young's modulus was 8.6 GPa and 9.3 GPa while the hardness was 5.7 GPa and 8.5 GPa, calculated for the first and second compressions, respectively. It can be observed that the Young's modulus, as well as the hardness of the particle, increased after consecutive compressions.

The same analysis was performed for the simulations. As in the experiment, no breakage in the structure of soot was observed during the simulated compression process. Figure 8 shows the change in particle height (a) and the height change relative to the initial particle size (b) after each compression step. Consistent with the experiment (see figure 9), the particle height and relative particle height both decrease with compression, indicative of permanent deformation after each compression step.

Figure 8(c) shows the force–displacement diagram and part (d) shows the elastic constant obtained from the slope of the unloading stage of the simulation from three consecutive compressions. These results also imply that the deformation of the model soot particle includes both elastic and plastic deformation. Most importantly, the elastic constant increases with compression cycle, which is consistent with what was observed during experimental tests, suggesting the model particle and the simulation process are physically realistic.

In order to confirm the behavior observed with a single SNP in both experiments and simulations, two or three consecutive compression experiments were performed on multiple SNPs under similar conditions to those described above. Details about the particles can be found in table 2 and in the supplementary material.

Figure 9(a) shows the *y*-size evolution of the particles. It can be seen that every particle suffers a permanent size change after every compression. The relative *y*-size change is displayed in figure 9(b). It can be observed that, on average, the *y*-size of a particle after the first compression is reduced by 21%. The size further decreases after the second compression by 35% on average. Although there is a relatively large change in the *y*-size, the particles do not break up upon compression.

Two other observations in the force–displacement diagrams in experiments (figure 9(c)) and simulations (figure 8(c)) are non-linearity and a decrease in the gap between loading and unloading curves after each compression step. These trends can be attributed to the conversion of some sp^2 hybridized carbon atoms to sp^3, as well as changes in the alignment of graphene sheets normal to the compression direction, both of which increase the elastic behavior of the material.

As presented for the case of particle D1A, the 'elastic constant' (the slope of the line fitted to the unloading part of the force–displacement data) shows an increase after the second compression compared with the first (figure 9(c) shows the force–displacement data for particle D1B).

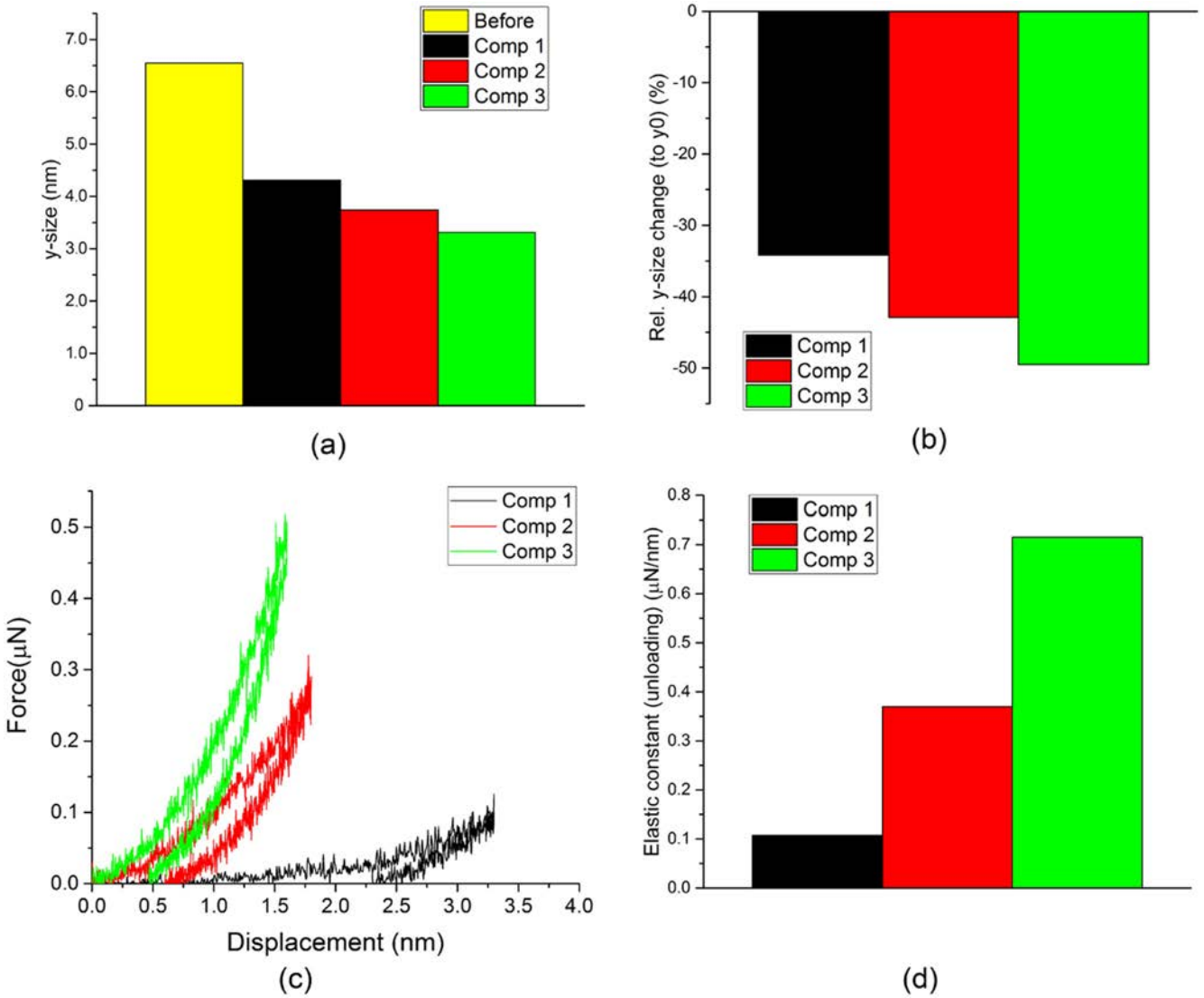

Figure 8. (a) Changes in height (*y*-size) of the modeled particle during each compression. (b) Relative change in height compared with the original size of the particle. (c) Force–displacement diagram during three consecutive compressions. (d) The elastic constant calculated from the slope of each unloading stage.

Figure 9(d) shows these 'elastic constants' for all the compressed particles. A clear trend can be observed: regardless of the size, shape or origin of the SNP, the 'elastic constant' increases after each consecutive compression.

The graphs displayed in figures 10(a) and (b) show the calculated Young's moduli and hardness values of the compressed particles from experiments. Similar to the 'elastic constant', the Young's modulus of the particles increases after consecutive compressions. On average, this value was 8.2 GPa during the first compression and 20.9 GPa during the second compression.

The same increasing trend can be observed for the calculated hardness values (see figure 10(b)). On average, a hardness of 4.9 GPa was calculated based on the first compression, and of 12.3 GPa on the second compression. On analyzing both the Young's modulus and hardness averages it should be noted that the third compression dataset was only available for one particle. Average values are not calculated in this case, although all parameters follow the trend observed during the first and second compressions.

The hardness of SNPs originating from diesel engines was measured by Jao *et al* [7] by recording the low-loss EELS spectra of the nanoparticles. According to the theory developed by Oleshko *et al* [41], the position of the plasmon peak in a low-loss EELS spectrum can be related to the hardness of the sample. The hardness values reported by Jao *et al* are in the range 8–14 GPa. Pavon used the same technique to characterize SNPs originating from diesel engines; she reports hardness values of between 6.8 and 12 GPa [42]. The hardnesses reported here from the experimental data for the diesel SNPs are in the range of 3–16 GPa. These values are in fairly good agreement, considering that they are the result of two independent techniques.

In their review article, Green *et al* [16] present abrasion as a wear mechanism of SNPs originating from diesel engines. Considering the hardness of the SNPs measured in

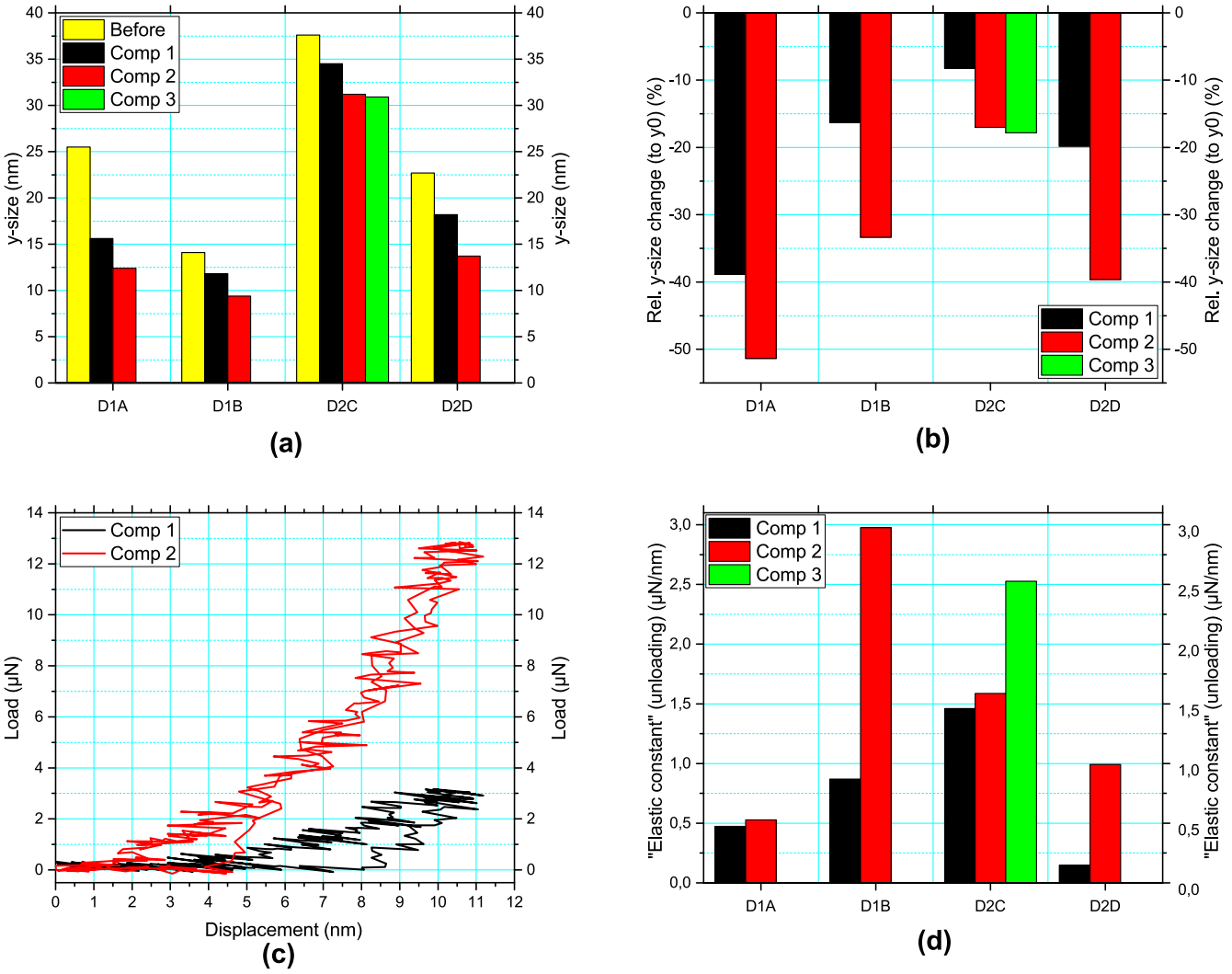

Figure 9. (a) The *y*-size evolution of the particles during compressions. (b) The relative *y*-size change compared with the original size of the particle. (c) The experimental force–displacement diagram during the two consecutive compressions for particle D1B. (d) The 'elastic constant' obtained by linear least squares fitting to the unloading data.

Table 2. The identification of different soot nanoparticles.

Sample reference	Particle reference
D1	D1A
D1	D1B
D2	D2C
D3	D2D[a]

[a] Particle D2D was collected from exhaust gases of a diesel engine vehicle test.

this work (in the range 3–16 GPa) and the hardness values of steel (a few GPa) or the hardness values of protective ZDDP films (2–5 GPa [43]), the abrasive wear mechanism is plausible inside a diesel internal combustion engine.

In order to better understand the increasing Young's modulus and hardness values, the structure of the SNPs was considered: an outer shell containing graphene-like layers and an inner core containing amorphous carbon [6]. It can be assumed that the soot is a mixture of carbon atoms having sp^2 and sp^3 hybridization states. The carbon allotrope in the pure sp^3 hybridization state (diamond) has a hardness of about 100 GPa while carbon in the pure sp^2 state (graphite) has a hardness of about 0.3 GPa. Energetically, the sp^3 state is more favorable. Taking all this into consideration, the following hypothesis was made: during compression, the hybridization state of a fraction of carbon atoms changes from sp^2 to sp^3, which in turn will contribute to the higher hardness values.

In order to test this hypothesis experimentally, EELS measurements were performed. The zero-loss and core-loss EELS spectra of the soot nanoparticle were recorded before the compression and after each compression. Using a method described by Daniels *et al* [44], a ratio proportional to the sp^2/sp^3 ratio (denoted as the '$\propto sp^2/sp^3$ ratio') could be calculated by fitting Gaussians in the core-loss spectrum to the peaks corresponding to the respective carbon hybridization states. In order to obtain absolute values for the sp^2 content

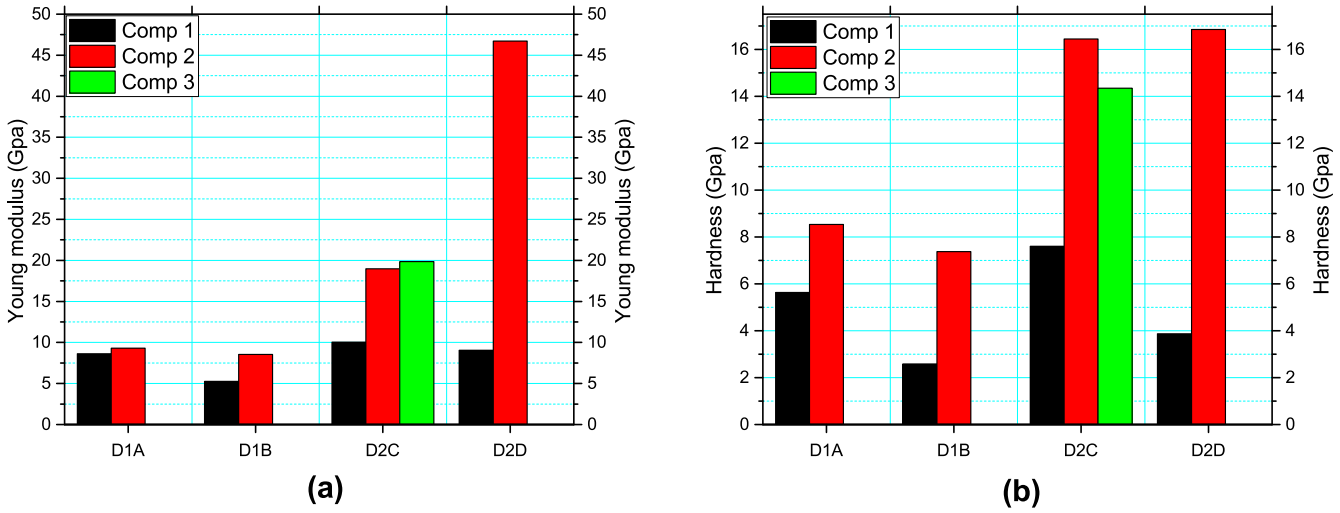

Figure 10. (a) The calculated Young's modulus and (b) hardness of the compressed particles.

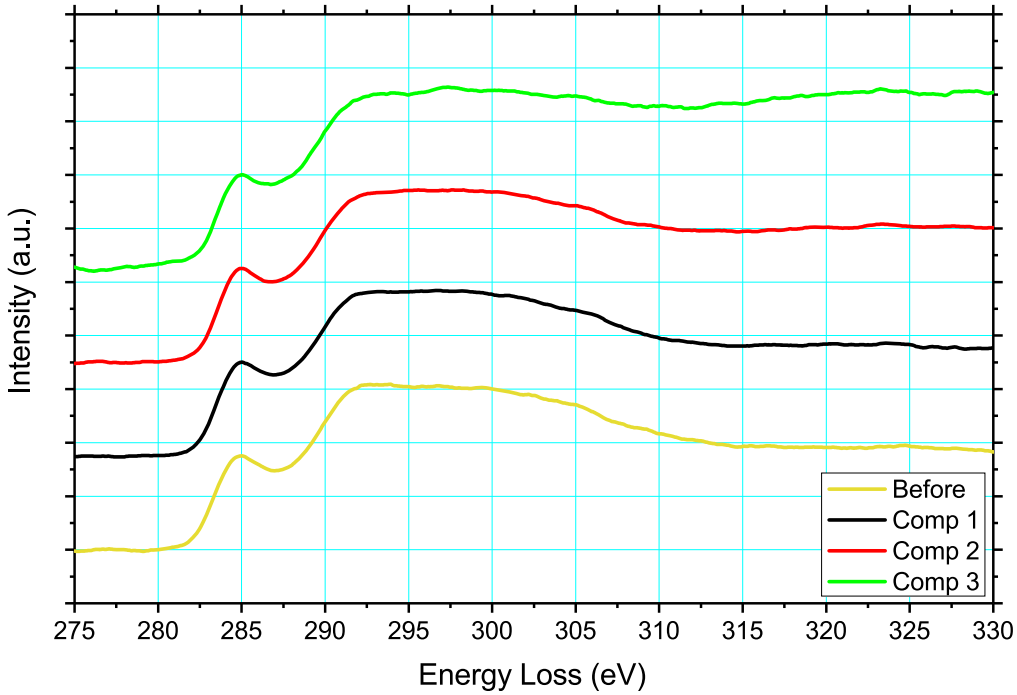

Figure 11. The EEL spectra of particle D2C recorded before and after each compression cycle. All spectra were background subtracted and normalized to the maximum intensity of the π^* peak. Plural scattering was removed by using the Fourier-ratio method. The π^* peak maxima were aligned on the energy loss axis.

calculation, a graphite standard needs to be used. In the absence of this, the calculated ratio still provides useful information in the form of the relative change of sp^2/sp^3 ratio as compared with the 'before compression' state of the particle.

The EELS dataset was collected on particle D2C (see figure 11). Figure 12 shows the measured and calculated parameters. The decreasing y-size of the particle, the increasing Young's modulus and the increasing hardness can be seen in figures 12(a)–(c). Figure 12(d) shows the evolution of the measured sp^2/sp^3 ratio. A decreasing tendency can be observed. The increasing tendencies observed for Young's modulus and hardness were consistent with the decreasing tendency of the sp^2/sp^3 ratio, which supports the above-stated hypothesis.

Figure 13(a) shows the estimated value of the hardness from simulations at the beginning and after each compression step. This graph shows an increasing trend in the hardness of the model particle after each compression. Thus, the simulations reproduced the same trend as the experiments. Furthermore, the hardness of the model SNP is comparable to the hardness values determined experimentally.

In the simulation, the sp^2/sp^3 ratio can be directly calculated based on the number of bonds of each carbon atom in

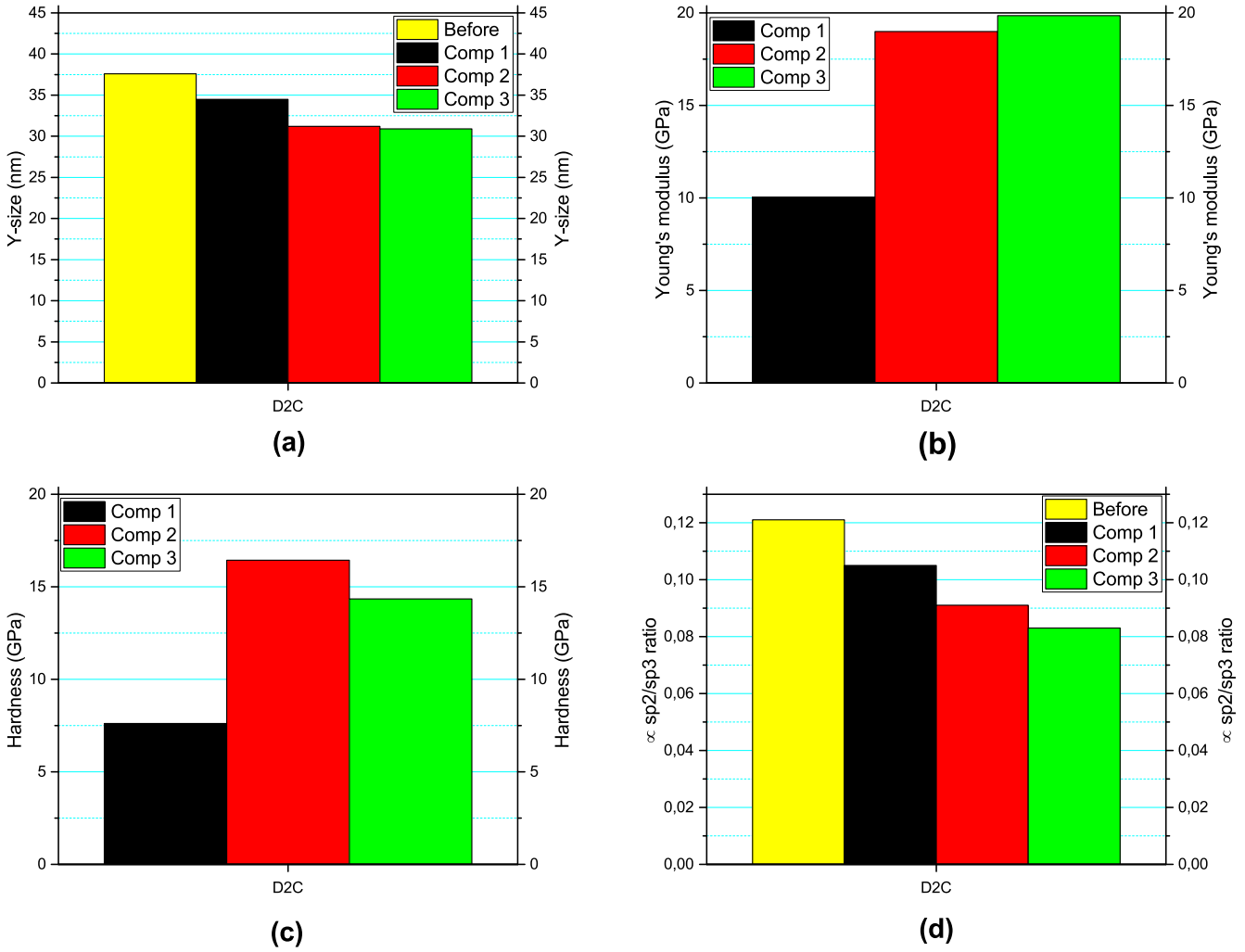

Figure 12. The measured parameters of particle D2C: (a) the *y*-size evolution; (b) the Young's modulus; (c) the hardness and (d) the sp^2/sp^3 ratio. Notice that the values shown in (d) are proportional to the actual sp^2/sp^3 ratio of the SNP.

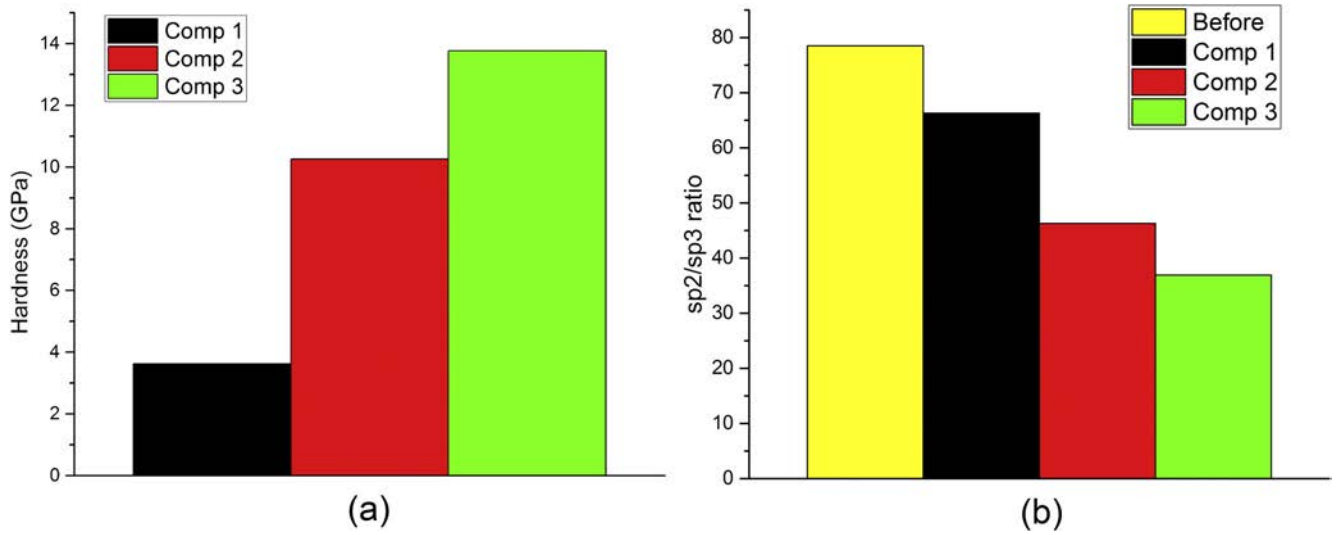

Figure 13. (a) Calculated hardness and (b) sp^2/sp^3 ratio in the model particle as a function of the simulation compression step.

the system. Figure 13(b) shows that the sp^2/sp^3 ratio decreases with compression steps, consistent with the results from the EELS analysis. The observed trend is due to an increase in the number of sp^3 hybridized carbon atoms, which results from the formation of new bonds between carbon atoms and their neighbors caused by compression.

Further, MD simulation results showed that the graphitic shell makes a smaller contribution to the decrease in sp^2/sp^3 ratio than the amorphous core. This is mainly because of the change in alignment of the graphene sheets at the top and bottom of SNP shell during compression, which will increase the elastic behavior in those areas. This change hinders the ability of these aligned graphene sheets to establish new bonds and deform permanently, as previously reported for carbonaceous lamellar structures under compression [45].

5. Conclusions

In situ compression tests were performed on SNPs originating from diesel engines. During compression, the nanoparticles exhibited elasto-plastic behavior, and they suffered permanent changes in shape and size. Further, the compressions resulted in a change of the structure of the SNPs: the exterior layers of the outer shell of the particle were 'smoothed' and the turbostratic or fulleneroid structure of the core almost disappeared. The calculated Young's moduli and hardness of the nanoparticles increased after consecutive compressions. EELS measurements confirmed a decrease in the sp^2/sp^3 ratio, which might explain the increase in hardness values. In the light of these results it can be stated that the SNPs which suffer repeated mechanical stress inside an internal combustion engine, due to their relatively high hardness, might affect the wear mechanism inside an engine. Molecular dynamics simulations complemented the experimental measurements. Compression of the soot model also resulted in an elasto-plastic behavior, which indicates the model is physically realistic. Simulation of consecutive compressions confirmed a permanent size change, an increasing trend of the elastic modulus and, at the same time, a decreasing sp^2/sp^3 ratio. Lastly, the high hardness values of the nanoparticles support the abrasive wear mechanism of SNPs.

Acknowledgments

This work was supported by LABEX iMUST (ANR-10-LABX-0064) of Université de Lyon, within the program 'Investissements d'Avenir' (ANR-11-IDEX-0007) operated by the French National Research Agency (ANR). Thanks are also due to CLYM for access to the ETEM microscope. The authors thank Dr Jean-Luc Loubet and Dr Julien Fontaine for valuable discussions.

ORCID iDs

Istvan Zoltan Jenei https://orcid.org/0000-0003-2021-4156

References

[1] Bardasz E A, Arters D C, Schiferl E A and Righi D W 1999 A comparison of gasoline direct injection and port fuel injection vehicles: part II—lubricant oil performance and engine wear *SAE Int.* **V108-4** 1999-01-1499
[2] Palmer H and Cullis C 1965 *Chem. Phys. Carbon* **1** 265
[3] Uy D, Ford M a, Jayne D T, O'Neill A E, Haack L P, Hangas J, Jagner M J, Sammut A and Gangopadhyay A K 2014 *Tribol. Int.* **80** 198–209
[4] Kawamura M, Ishiguro T and Morimoto H 1987 *Lubric. Eng.* **43** 572–5
[5] Patel M, Azanza Ricardo C L, Scardi P and Aswath P B 2012 *Tribol. Int.* **52** 29–39
[6] La Rocca A, Di Liberto G, Shayler P J and Fay M W 2013 *Tribol. Int.* **61** 80–7
[7] Jao T C, Li S, Yatasumi K, Chen S J, Csontos A A and Howe J M 2004 *Lubric. Sci.* **16** 111–26
[8] Sharma V, Uy D, Gangopadhyay A, O'Neill A, Paxton W A, Sammut A, Ford M A and Aswath P B 2016 *Carbon* **103** 327–38
[9] Violi A and Izvekov S 2007 *Proc. Combust. Inst.* I **31** 529–37
[10] Omidvarborna H, Kumar A and Kim D S 2015 *Renew. Sustain. Energy Rev.* **48** 635–47
[11] Xi J and Zhong B J 2006 *Chem. Eng. Technol.* **29** 665–73
[12] Ghaednia H and Jackson R L 2013 *J. Tribol.* **135** 041603
[13] Duncan D A, Reed M, Szabo A L and Williams L 2004 Soot related viscosity increase—a comparison of the Mack T-11 engine test to field performance *SAE Int.* **V113-4** 2004-01-3009
[14] George S, Balla S and Gautam M 2007 *Wear* **262** 1113–22
[15] Gautam M, Chitoor K, Durbha M and Summers J C 1999 *Tribol. Int.* **32** 687
[16] Green D A and Lewis R 2008 *Proc. Inst. Mech. Eng.* D **222** 1669–89
[17] Ratoi M, Castle R C, Bovington C H and Spikes H A 2004 *Lubric. Sci.* **17** 25–43
[18] Motamen Salehi F, Morina A and Neville A 2017 *Tribol. Int.* **115** 285–96
[19] Wall M A and Dahmen U 1997 *Microsc. Microanal.* **3** 593
[20] Bobji M, Pethica J and Inkson B 2005 *J. Mater. Res.* **20** 2726–32
[21] Nafari A, Karlen D, Rusu C, Svensson K, Olin H and Enoksson P 2008 *J. Microelectromech. Syst.* **17** 328–33
[22] Warren O L, Shan Z, Asif S A S, Stach E A, Morris J W and Minor A M 2007 *Mater. Today* **10** 59–60
[23] Yu Q, Legros M and Minor A M 2015 *MRS Bull.* **40** 62–70
[24] Howe J, Mori H and Wang Z 2008 *MRS Bull.* **33** 115–21
[25] Minor A M, Morris J W and Stach E A 2001 *Appl. Phys. Lett.* **79** 1625–7
[26] Stach E A *et al* 2001 *Microsc. Microanal.* **7** 507–17
[27] Asthana A, Momeni K, Prasad A, Yap Y K and Yassar R S 2011 *Nanotechnology* **22** 265712
[28] Deneen J, Mook W M, Minor A, Gerberich W W and Carter C B 2006 *J. Mater. Sci.* **41** 4477–83
[29] Lahouij I, Dassenoy F, Vacher B, Sinha K, Brass D A and Devine M 2014 *Tribol. Lett.* **53** 91–9

[30] Calvie E *et al* 2014 *Mater. Lett.* **119** 107–10
[31] Colla M S, Amin-Ahmadi B, Idrissi H, Malet L, Godet S, Raskin J P, Schryvers D and Pardoen T 2015 *Nat. Commun.* **6** 5922
[32] Vander Wal R L, Tomasek A J, Street K, Hull D R and Thompson W K 2004 *Appl. Spectrosc.* **58** 230–7
[33] Martínez L, Andrade R, Birgin E G and Martínez J M 2010 *J. Comput. Chem.* **30** 2157–64
[34] Senftle T P *et al* 2016 *NPJ Comput. Mater.* **2** 15011
[35] van Duin A C T, Dasgupta S, Lorant F and Lorant A G W 2001 *J. Phys. Chem.* A **105** 9396–409
[36] Shin Y K, Gai L, Raman S and Van Duin A C T 2016 *J. Phys. Chem.* A **120** 8044–55
[37] Kamat A M, van Duin A C T and Yakovlev A 2010 *J. Phys. Chem.* A **114** 12561–72
[38] Rissler J, Messing M E, Malik A I, Nilsson P T, Nordin E Z, Bohgard M, Sanati M and Pagels J H 2013 *Aerosol Sci. Technol.* **47** 792–805
[39] Srivastava D, Agarwal A K and Gupta T 2011 *Aerosol Air Qual. Res.* **11** 915–20
[40] Plimpton S 1995 *J. Comput. Phys.* **117** 1–19
[41] Oleshko V P, Murayama M and Howe J M 2002 *Microsc. Microanal.* **8** 350–64
[42] Pavon D 2007 Caractérisation des dépôt sur les pistons *PhD Thesis* Ecole Centrale de Lyon, LTDS
[43] Aktary M, McDermott M T and McAlpine G A 2002 *Tribol. Lett.* **12** 155–62
[44] Daniels H, Brydson R, Rand B and Brown A 2007 *Phil. Mag.* **87** 4073–92
[45] Gao H L *et al* 2016 *Nat. Commun.* **7** 12920